Breakdown of aerodynamic interactions for the lateral rotors on a compound helicopter

Stokkermans, Tom; Veldhuis, Leo; Soemarwoto, Bambang; Fukari, Raphaël; Eglin, Paul

DOI
10.1016/j.ast.2020.105845

Publication date
2020

Document Version
Final published version

Published in
Aerospace Science and Technology

Citation (APA)
Stokkermans, T., Veldhuis, L., Soemarwoto, B., Fukari, R., & Eglin, P. (2020). Breakdown of aerodynamic interactions for the lateral rotors on a compound helicopter. *Aerospace Science and Technology*, *101*, Article 105845. https://doi.org/10.1016/j.ast.2020.105845

Aerospace Science and Technology 101 (2020) 105845

Contents lists available at ScienceDirect

Aerospace Science and Technology

www.elsevier.com/locate/aescte

Breakdown of aerodynamic interactions for the lateral rotors on a compound helicopter[☆],[☆☆]

Tom Stokkermans[a,*], Leo Veldhuis[a], Bambang Soemarwoto[b], Raphaël Fukari[c], Paul Eglin[c]

[a] Delft University of Technology, Delft, the Netherlands
[b] Netherlands Aerospace Centre NLR, Amsterdam, the Netherlands
[c] Airbus Helicopters, Marignane, France

ARTICLE INFO

Article history:
Received 6 August 2019
Received in revised form 17 February 2020
Accepted 31 March 2020
Available online 28 April 2020
Communicated by George Barakos

ABSTRACT

Auxiliary lift and/or thrust on a compound helicopter can introduce complex aerodynamic interactions between the auxiliary lift and thrust components and the main rotor. In this study high-fidelity computational fluid dynamics analyses were performed to capture the various aerodynamic interactions which are occurring for the Airbus RACER compound helicopter, featuring a box-wing design for auxiliary lift in cruise and wingtip-mounted lateral rotors in pusher configuration for auxiliary thrust in cruise and counter-torque in hover. Although the study was limited to a specific geometry, the effects and phenomena are expected to be to some extent applicable in general for compound helicopters and wingtip-mounted rotors in pusher configuration. A quantitative indication of the aerodynamic interaction effects could be established by leaving away different airframe components in the simulations. The downwash of the main rotor was found to cause a small negative angle of attack in cruise for the wings and lateral rotors and impinged directly on the lateral rotors in hover, resulting in moderate to very significant sinusoidally varying blade loading. The wing increased lateral rotor propulsive efficiency in cruise through its wingtip rotational flowfield and to a lesser extent through its wake. An upstream effect of the lateral rotors on the wing loading was also found. In hover the wing caused a net increase in left lateral rotor thrust as the deflection of the main rotor flow towards the rotor resulted in a local thrust decrease and the low momentum inflow to the rotor from the wake of the wing resulted in a local thrust increase. A small thrust decrease for the right lateral rotor was found due to the wing disturbing its slipstream as this rotor produced reversed thrust. In general, very significant aerodynamic interaction effects can be expected when a main rotor, lateral rotors and wing are in proximity to each other.

1. Introduction

There is a growing need for aircraft with vertical take-off and landing capability that can go fast and far [1]. While helicopters are excellent for vertical take-off and landing, they only have a limited maximum speed: The asymmetric flow condition of the main rotor at high speed causes compressibility effects on the advancing blade side and stall on the retreating blade side of the main rotor that limit its lifting and propulsive capability [2,3]. A compound helicopter overcomes the main rotor limitation at high speed by auxiliary lift and thrust devices [1,2]. An example of such a compound helicopter concept is the Airbus RACER (Rapid And Cost-Effective Rotorcraft) [4,5], optimized for a high cruise speed of 220 kts. In Fig. 1 a sketch is shown of the helicopter, without main rotor and tailplanes. Supporting the main rotor, auxiliary lift in the cruise condition is provided by a box-wing, while wingtip-mounted lateral rotors in pusher configuration generate a major portion of the required thrust. Furthermore, these lateral rotors provide counter-torque in the hover condition to balance the main rotor torque. In the cruise condition, the vertical fins (not shown) produce all the counter-torque. They are also fitted with flaps in order to adjust the counter-torque as function of e.g. airspeed, air density and main rotor torque. For brevity, from this point on, lateral rotors will be referred to as propellers. Compared to a single wing design, the box-wing design reduces the overall surface affected by the downwash of the main rotor in hover, while delivering the required lift

---

[☆] Funding: This project has received funding from the Clean Sky 2 Joint Undertaking under the European Union's Horizon 2020 research and innovation programme under grant agreement No. 685569 — PROPTER — H2020-CS2-CFP01-2014-01.

[☆☆] This paper reflects only the author's view and the JU is not responsible for any use that may be made of the information it contains.

[*] Corresponding author.
E-mail address: T.C.A.Stokkermans@tudelft.nl (T. Stokkermans).

https://doi.org/10.1016/j.ast.2020.105845

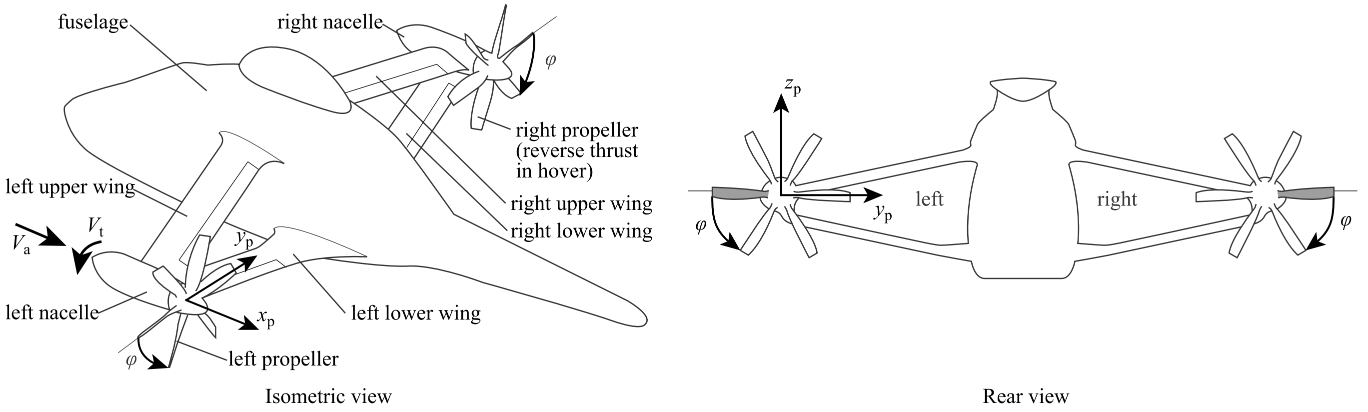

Fig. 1. Sketches of the Airbus RACER without main rotor and tailplanes. Propeller blade phase angle φ and axial and tangential velocity components V_a and V_t are indicated.

in cruise. It can also improve lift-over-drag ratio compared to a planar wing design [6].

Because of the close proximity of the box-wing and main rotor, the propellers experience various aerodynamic interactions. These interactions significantly differ for each flight condition. The propeller installation effects for this compound helicopter have been described by Stokkermans et al. [7] and to some extent by Wentrup et al. [8]. Furthermore, the interaction of a wingtip-mounted pusher-propeller with the upstream wing has been studied for planar wings by Refs. [9–12]. The extensive experimental study of Bain and Landgrebe [13] covers main rotor–wing aerodynamic interaction and main rotor–propeller aerodynamic interaction for a compound helicopter, treating both cases separately. The focus of that study was on the blade moments which the main rotor and propeller experience. Main rotor–wing interaction was also investigated by Lynn [14] and specifically for the RACER, the design of the box-wings with main rotor interaction is covered by Wentrup et al. [8].

In the review of lessons learned from the compound helicopter studies done by NASA and the US Army by Yeo [1], the need is stressed for high-fidelity computational fluid dynamics analyses to capture the various aerodynamic interactions which are occurring for compound helicopters. According to Yeo [1], these aerodynamic characteristics could then be used for calibration of lower order models, and layout and shape refinement. In line with this need, as part of the Clean Sky 2 PROPTER project (Support to aerodynamic analysis and design of propellers of a compound helicopter), in this article a high fidelity breakdown is presented of the various aerodynamic interaction effects between the propellers, the box-wings and the main rotor downwash. These effects include local changes in dynamic pressure and angle of attack from vortices, boundary layers and rotor momentum sources. The focus of this article is on the resulting changes in loading and efficiency of the propellers and lift and drag of the box-wing.

2. Computational setup

The aerodynamic interaction effects were investigated through a series of Reynolds-averaged Navier-Stokes (RANS) CFD simulations. In Fig. 2 the various simulated configurations are depicted. By leaving away different airframe components in the simulations, a quantitative indication of the aerodynamic interaction effects could be established. The model was simplified by removal of the tail unit and the time-averaged effect of the main rotor was introduced by an actuator disk implementation, similar to e.g. Batrakov et al. [15], which consists of radially and circumferentially varying momentum and energy jump conditions based on provided blade loading distributions. Note that rotor and rotor-head wake interactions with the tail unit and resulting design optimisation of the tail unit have been studied separately by Lienard et al. [5] and Salah el Din et al. [16] respectively.

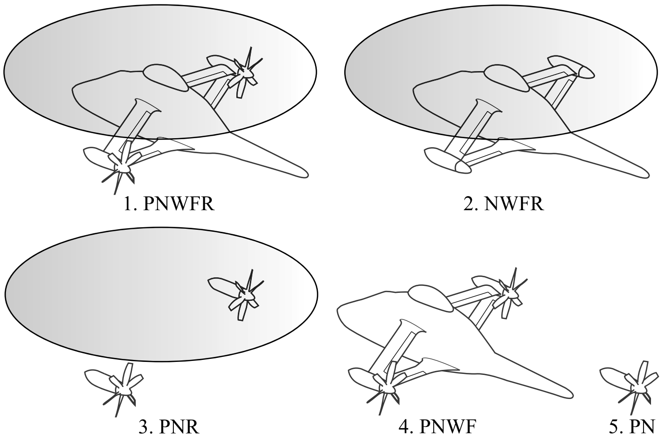

Fig. 2. The five different simulated configurations including labels (P: propeller; N: nacelle; W: wing; F: fuselage; R: rotor).

Adaptive mesh refinement techniques such as described by Öhrle et al. [17] would enable the full simulation of the main rotor with reduced computational cost, but for this project a large quantity of simulations were needed to study the interactions in the various configurations and operating conditions, necessitating the more computational cost effective actuator disk approach. Of course, one should consider that this setup neglects any of the transient effects that the main rotor blade tip vortices and wakes have on the propeller loading as e.g. described by Thiemeier et al. [18]. Furthermore, no interaction effect of the propeller on the main rotor loading is present as the actuator-disk loading is prescribed. As is known from the extensive experimental investigation of Bain and Landgrebe [13], a propeller close to the main rotor may affect the rotor flapping amplitude and bending moments due to its pressure field, and as such the main rotor loading. However, the actuator-disk loading includes the asymmetry occurring in the loading on the main rotor in forward flight between the advancing and retreating blade side and the radial non-uniformity present in the loading on rotors and as such represents the time-averaged effect of the main rotor on the flowfield accurately.

2.1. Flow solver, domain and boundary conditions

The flow solver used for these simulations was ENFLOW, a multiblock structured solver by NLR [19–22]. The RANS equations were discretized in space by a second-order cell-centred finite-volume method, using central differences and artificial diffusion.

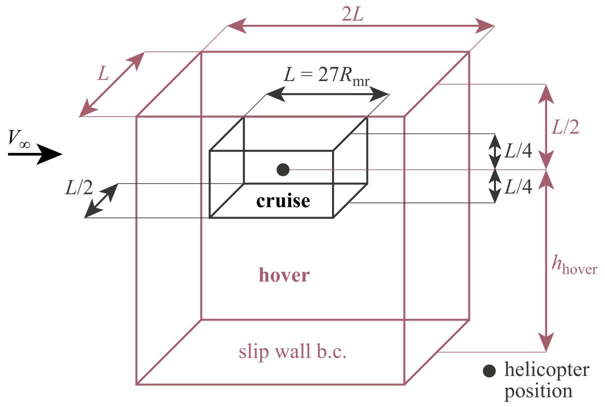

Fig. 3. Comparison of the computational domain for the cruise condition and enlarged domain for the hover condition.

The steady flow equations were solved by a multi-grid scheme, using as relaxation operator a Runge-Kutta scheme. For transient solutions, the flow equations were integrated in time by a second-order implicit scheme, using the dual-time stepping method. A timestep equivalent to 1 deg of propeller rotation was used for the final results as commonly found in propeller research [23,24]. To model turbulence in the cruise condition, an explicit algebraic Reynolds-stress was selected for the Reynolds-stress tensor (EARSM), combined with the TNT $k-\omega$ model to determine the relevant turbulent time and length scales [25]. For the hover condition the $k-\omega$ SST model was used to promote convergence of this complex flowfield [26]. For the PN configuration, transient simulations were performed whenever the propeller was at angle of attack. For zero angle of attack, a single blade passage was modelled in a steady simulation with cyclic periodic boundary conditions to reduce computational cost.

For the PNWFR, PNR and PNWF configurations, transient simulations were performed, while the NWFR configuration was simulated steady to reduce computational cost. The domain dimensions for these simulations are depicted in Fig. 3. For the cruise condition, the dimension in the freestream direction L was chosen larger than the other dimensions to diminish the effect of the boundary conditions on the flowfield near the helicopter. Furthermore, on all boundaries, general free stream boundary conditions were prescribed based on Riemann invariants. The freestream airspeed in the cruise condition was set to 220 kt (113.2 m/s) with a static temperature of 276.3 K and density of 1.024 kg/m^3. For the hover condition, a larger domain was required to prevent unwanted recirculation and thus unwanted influence of the boundary conditions on the flowfield near the helicopter. The bottom boundary condition was placed at a distance equal to the hover altitude h_{hover} and modelled as a slip wall. A very small freestream velocity was prescribed to further reduce recirculation in the domain and the static temperature was set to 306.2 K and density to 1.112 kg/m^3.

Transient solutions were sought after which were periodic with the propeller blade passage frequency. The procedure to obtain this periodic solution differed for each flight condition. For the cruise condition the following procedure was applied over three grid levels (coarse, medium and fine):

1. Steady coarse grid simulation for 1,000 iterations.
2. Continue with transient coarse grid simulation for 4 propeller rotations.
3. Continue with transient medium grid simulation for 3 propeller rotations.
4. Continue with transient fine grid simulation for 2 propeller rotations.

The hover configuration required a different recipe to avoid divergence in the solver and to reach periodic behaviour with the blade passage frequency. It was found that to reach periodic behaviour for this flight condition, many propeller rotations were required as the flowfield is induced by the main rotor actuator disk and propellers. A larger timestep equivalent to 10 deg of propeller rotation was used to reach the periodic behaviour with a relatively low computational cost. Eventually a small time step equivalent to 1 deg of propeller rotation was again used to obtain the desired temporal resolution:

1. Steady coarse grid simulation for 10,000 iterations.
2. Continue with steady medium grid simulation for 4,000 iterations.
3. Continue with steady fine grid simulation for 2,000 iterations.
4. Continue with transient fine grid simulation for 30 propeller rotations with 10 deg equivalent timestep.
5. Continue with transient fine grid simulation for 4 propeller rotations with 1 deg equivalent timestep.

To obtain time-averaged results, a final blade-passage (60 deg of propeller rotation) was simulated, over which all quantities of interest were averaged. The computational cost of a PNWFR configuration simulation was approximately 180 hr on 240 cores of a modern HPC cluster for the cruise condition and the double for the hover condition.

2.2. Grid and grid dependency study

Block structured grids were constructed and the propellers and spinner were in a separate domain from the rest of the airframe to allow propeller motion with a sliding mesh interface. A sliding mesh interface was also present around the propeller blade to allow change of propeller blade pitch without redefinition of the structured grid. The fine grid contained about 153 million cells for the cruise condition and 163 million cells for the hover condition. The grid size of the hover condition was slightly different as a result of the enlarged domain and the need for a different first layer thickness. In order to comply with the turbulence models, the dimensionless wall distance y^+ on all no-slip walls of the model was less than one.

In order to assess the dependency of the results on the grid, the grid convergence index (GCI) was evaluated. The procedure from Celik et al. [27] was followed. For a quantity of interest, ϕ_1 is its value on the fine grid, ϕ_2 on the medium grid and ϕ_3 on the coarse grid. The medium and coarse grid were obtained by structured grid coarsening. The apparent order of the scheme p based on the solution of the quantity of interest on the three grids is given by:

$$p = \frac{1}{\ln(r_{21})}|\ln(\varepsilon_{32}/\varepsilon_{21})| \quad \text{with} \quad \varepsilon_{32}/\varepsilon_{21} = \frac{\phi_3-\phi_2}{\phi_2-\phi_1} \tag{1}$$

where r_{21} is the grid refinement ratio from the medium to the fine grid, 2 in this case. Note that this procedure only works if the ratio of $\varepsilon_{32}/\varepsilon_{21}$ is positive. Negative values indicate oscillatory convergence. The fine-grid convergence index with a 1.25 safety factor is given by:

$$\text{GCI}^{21}_{\text{fine}} = \frac{1.25e^{21}_a}{r^p_{21}-1} \quad \text{with} \quad e^{21}_a = |\frac{\phi_1-\phi_2}{\phi_1}| \tag{2}$$

with e^{21}_a the approximate relative error. Since the grid is refined in a structured manner and the solver is second order accurate, also an error based on Richardson extrapolation can be calculated, where $p=2$ in the previous equations. The fine grid relative error based on Richardson extrapolation is [28]:

Table 1
Grid convergence study results in the cruise condition based GCI and Richardson extrapolation.

	left propeller		right propeller		airframe	
	thrust	power	thrust	power	lift	drag
$\varepsilon_{32}/\varepsilon_{21}$	9.2	30.4	7.9	12.4	5.2	4.3
p	3.2	4.9	3.0	3.6	2.4	2.1
$\mathrm{GCI}^{21}_{\mathrm{fine}}$ (%)	0.1	0.0	0.2	0.0	1.4	6.9
E_1 (%)	0.2	0.0	0.4	0.1	1.6	6.2

Table 2
Grid convergence study results in the hover condition based GCI and Richardson extrapolation.

	left propeller		right propeller		airframe	
	thrust	power	thrust	power	lift	drag
$\varepsilon_{32}/\varepsilon_{21}$	3.0	6.6	8.3	7.9	-1.4	1.9
p	1.6	2.7	3.1	3.0	0.5	1.0
$\mathrm{GCI}^{21}_{\mathrm{fine}}$ (%)	0.7	0.3	0.1	0.2	-*	44.2
E_1 (%)	0.4	0.5	0.1	0.4	2.3	11.1

* oscillatory convergence.

$$E_1 = \frac{e_a^{21}}{2^2 - 1} \tag{3}$$

The advantage of this later uncertainty estimate is that it does not depend on the coarse grid, which might be out of the asymptotic range.

A summary of the grid-dependent uncertainties is given in Tables 1 and 2 for the cruise and hover condition respectively. Note that the airframe is composed of the fuselage, box-wings and nacelles. In the cruise and hover conditions the uncertainties estimated for the time-averaged propeller performance quantities are relatively small. For the airframe lift and drag somewhat larger uncertainties are estimated. In the cruise condition, this is mainly due to flow separation from the exhausts on the rear of the fuselage, since no active flow was simulated through the exhausts. In the hover condition, the largely separated flow from the leading and trailing edges of the wings, due to the very large inflow angle by the main rotor downwash, is the main cause of uncertainty. This flow separation is later discussed in Section 3.2. Note that the large GCI uncertainty for the airframe drag in the hover condition is a result of the very low apparent order of 1.0, which may be caused by the coarse grid being outside of the asymptotic range. The Richardson extrapolation uncertainty estimate E_1 is significantly lower for this quantity. Overall, as the focus of this study is on the propeller performance, the uncertainties were deemed acceptable.

3. Results

Since the interactions are significantly different, the results for the cruise condition and hover condition are treated separately in the next two sections.

3.1. Cruise condition

In the cruise condition, the propellers experience the rotational flowfield at the wingtip and are close to the main rotor slipstream. In this condition, the main rotor and propellers operate at an advance ratio (defined as $V_\infty/(\omega R)$ with ω in rad/s) above 0.5. In Fig. 4 this situation is sketched schematically and in Fig. 5 the flowfield through the left propeller is visualised by means of streamtraces with velocity contours. The respective influence of the wings and main rotor on the propeller performance is treated in this section. As well, the upstream influence of the propellers on the wings is discussed. Mainly results for the left propeller are given, since the results in this flight condition are qualitatively similar for both propellers. All results are at zero angle of attack and sideslip unless stated otherwise.

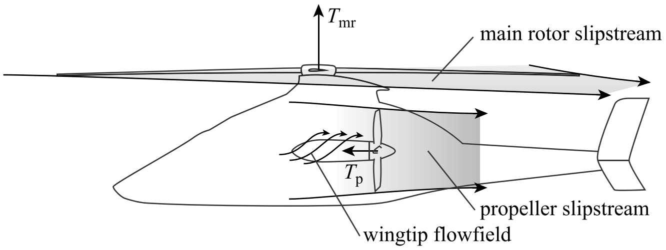

Fig. 4. Sketch of main rotor, box-wing and propeller aerodynamic interaction in cruise, indicating the direction of the main rotor thrust T_{mr} and propeller thrust T_{p}.

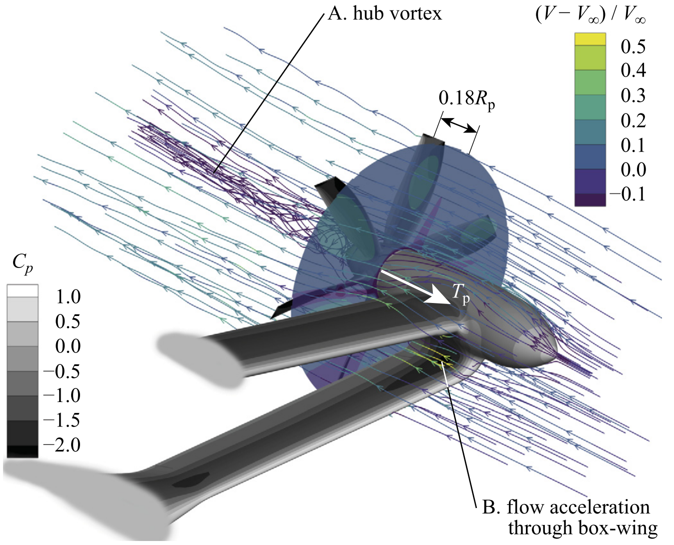

Fig. 5. For the PNWFR configuration in cruise, the flowfield is visualised through the left propeller, with velocity contours on streamtraces and on a plane $0.18R_{\mathrm{p}}$ upstream of the propeller. Only the left box-wing, nacelle and propeller are shown, marked with contours of the pressure coefficient $C_p = (p - p_\infty)/q_\infty$.

Table 3
Time-averaged left propeller performance for the PNR and PNWFR configurations relative to the PN configuration in cruise.

	PNR	PNWFR
ΔT	+2.9%	+0.7%
ΔP	+2.2%	−7.8%
$\Delta \eta_{\mathrm{p}}$	+1.0%	+7.0%

In Table 3 the left propeller performance is given for the PNR and PNWFR configuration relative to the performance at zero angle of attack for the PN configuration. For the PN configuration, the blade pitch was trimmed to a specific cruise thrust target. For the PNR configuration, this blade pitch angle was maintained to see directly the effect of the main rotor slipstream on the propeller performance. However, for the PNWFR configuration the blade pitch angle was trimmed by a series of simulations at a reduced grid, in order to arrive at a thrust close to the initial target. The reason for trimming is that the interaction with the wing increases the propeller thrust drastically, as will be explained later. The rotational speed and freestream velocity were maintained for both configurations. From the PNR configuration results, conclusions can be drawn on the effect of the main rotor on the propeller performance. In this configuration the propeller thrust T and shaft power

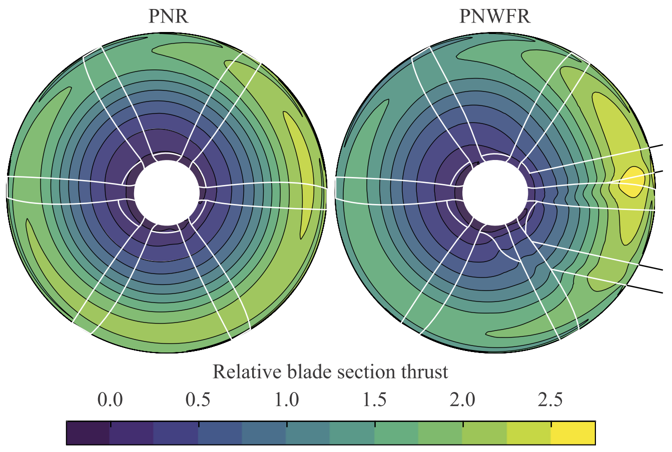

Fig. 6. The blade section thrust relative to the time-averaged blade thrust is plotted for each circumferential position of the left propeller in cruise. The effect of the wings is shown by means of comparison of the PNR and PNWFR configuration.

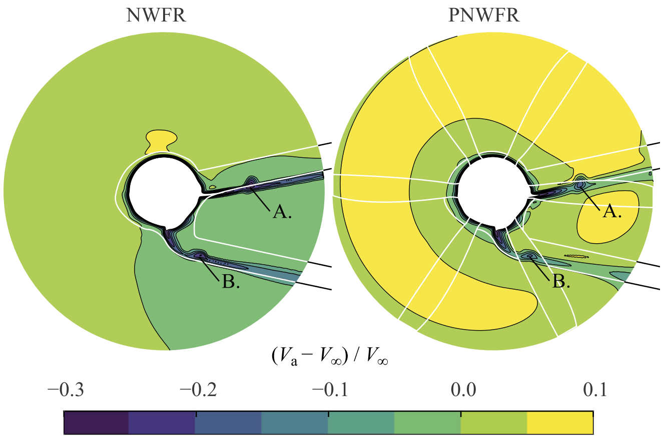

Fig. 7. Time-averaged axial velocity component is plotted on the plane visualised in Fig. 5, upstream of the left propeller in cruise. The effect of the propeller is shown by means of comparison of the NWFR and PNWFR configuration. Annotation A. and B. indicate the effect of the upper and lower wing flap edge gap.

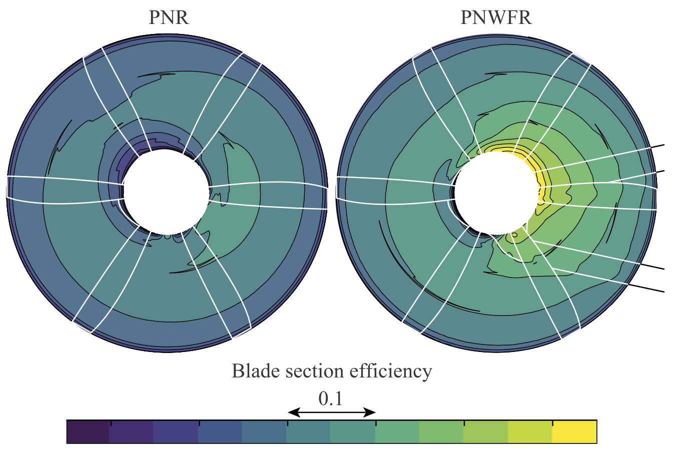

Fig. 8. The blade section efficiency $T'V_\infty/P'$ is plotted for each circumferential position of the left propeller in cruise. The effect of the wings is shown by means of comparison of the PNR and PNWFR configuration.

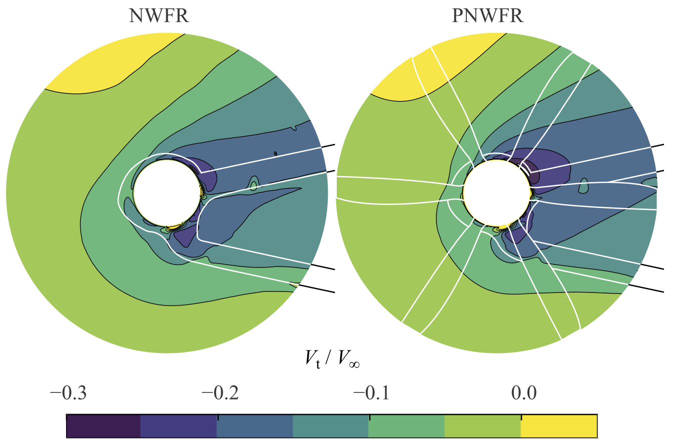

Fig. 9. Time-averaged tangential velocity component is plotted on the plane visualised in Fig. 5, upstream of the left propeller in cruise. The effect of the propeller is shown by means of comparison of the NWFR and PNWFR configuration.

P is increased as the propeller experiences a non-zero angle of attack from the potential effect of the main rotor and its slipstream. However, note that no main rotor slipstream impingement on the propeller disk occurs. The propulsive efficiency $\eta_p = TV_\infty/P$ is slightly increased as well by the same mechanism. This main rotor effect is slightly reduced for the right propeller, since it experiences a reduced downwash on the retreating blade side of this clockwise turning main rotor, confirming the findings by Wentrup et al. [8].

For the PNWFR configuration, a reduction in blade pitch angle was required to approximately maintain the thrust target as set for the PN configuration. The propulsive efficiency is significantly increased by 7% as a result of installation. As it was shown that for the PNR configuration the propulsive efficiency was slightly increased as well, part of this 7% increase is a result of the angle of attack induced by the main rotor.

To investigate where the differences in propeller performance for the PNR and PNWFR configuration originate, in Fig. 6 contour plots of the blade section thrust are shown for the left propeller. The white outline of the upstream box-wing enables correlation of the thrust variation with the wing location. In the PNR configuration the propeller blades experience a sinusoidal thrust variation in time, which is typical for a propeller at angle of attack. The maximum blade thrust is experienced when the blade moves up, because then the angle of attack effect of the main rotor downwash results in the largest blade section angle of attack. This confirms the observation by Wentrup et al. [8] for the same compound helicopter configuration. For the PNWFR configuration, additional non-uniformities are present. A maximum in blade section thrust is found around blade phase angle $\varphi = 180$ deg as defined in Fig. 1. This maximum occurs when the propeller blade is downstream of the upper wing. A sudden increase in thrust is also noticeable in the proximity of the lower wing. Both effects are explained below.

The axial velocity component V_a upstream of the propeller is plotted in Fig. 7 as defined in Fig. 1. It is plotted on the plane that was visualised in Fig. 5. Contour plots for the NWFR and PNWFR configuration are given, so without and with the propeller present. At the location of the peaks in thrust due to the box-wing in Fig. 6, a clear velocity deficit of the wake of the wings can be distinguished in the axial velocity field. Especially noticeable are the deficits at the location of the flap edge gaps indicated by annotations A. and B. The axial velocity deficit results in a local advance ratio reduction and thus thrust increase. Comparing the contour plots for the NWFR and PNWFR configuration, the upstream acceleration of the flow induced by the propeller loading is clearly visible, resulting in strong flow acceleration between the wings as annotated by label B in Fig. 5.

Pusher-propellers mounted at the tip of planar wings are associated with beneficial interaction effects in terms of propulsive efficiency, as is known from i.e. Refs. [9–12]. To show where the

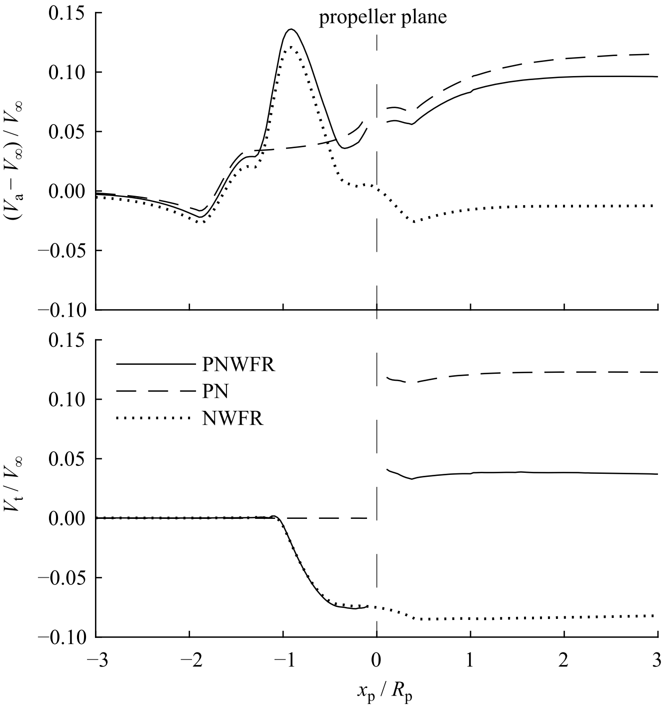

Fig. 10. For three configurations, PNWFR, PN and NWFR, the radially and circumferentially averaged axial and tangential velocity distribution through the left propeller approximate streamtube is plotted in cruise. The streamtube was approximated by a cylinder of radius equal to the propeller radius from 3 radii upstream to 3 radii downstream of the propeller.

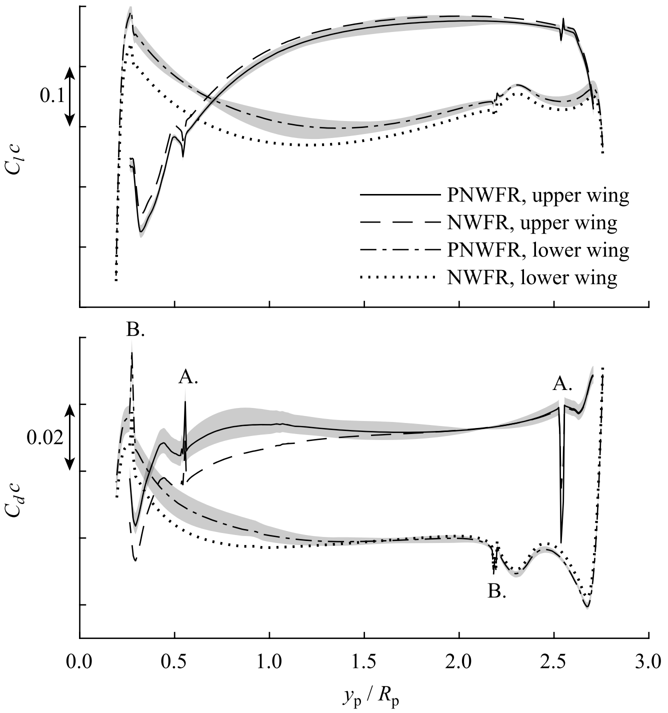

Fig. 11. Time-averaged wing loading comparison between PNWFR and NWFR configuration for the left wing in cruise, with coordinate y_p as defined in Fig. 1 and c the wing chord. Shaded area indicates time-variation. Annotation A. and B. indicate the effect of the upper and lower wing flap edge gap.

propulsive efficiency increase is coming from between the PNR and PNWFR configuration, in Fig. 8 a comparison of the blade section efficiency over the propeller disk is given. This is defined as the ratio of blade section contribution to thrust T' and blade section contribution to power P', multiplied by the freestream velocity magnitude V_∞. Although over the entire disk the blade section efficiency is raised for the PNWFR configuration compared to the PNR configuration, especially on the inboard side of the propeller disk and for blade sections at low radii a large increase can be noticed, as explained below.

The distribution of efficiency increase corresponds directly to the negative tangential velocity field shown in Fig. 9, as defined in Fig. 1 with the tangential component positive in the direction of propeller rotation. This negative tangential velocity is resulting from the pressure difference between the pressure side of the lower wing and suction side of the upper wing. The negative tangential velocity component increases the propeller blade section angle of attack and tilts the section lift more in the direction of the thrust and less in the tangential direction, reducing the contribution to the torque or shaft power. Comparing the contour plots for the NWFR and PNWFR configuration, a small upstream effect of the propeller can be noticed by an increase of the negative tangential velocity. Since a propeller does not induce an upstream tangential velocity field, this change in tangential velocity is likely a result from a change in wing loading and its induced tangential velocity field.

To qualitatively show how the aerodynamic interactions change the flowfield through the propeller, in Fig. 10 velocity components through the approximated streamtube of the left propeller are plotted for the PNWFR, PN and NWFR configuration. The streamtube is approximated by a cylinder with a radius equal to the propeller radius and quantities are time- and space-averaged over disks from $3R_p$ upstream to $3R_p$ downstream of the propeller. For the PNWFR and NWFR configuration, a large peak in axial velocity can be noticed upstream of the propeller, which is a result of the acceleration of the flow around the wings, since the streamtube intersects part of the wings. This acceleration is also visible in the velocity contours on the streamtraces in Fig. 5 and in the reduced pressure coefficient on the wing and nacelle surface, especially in between the upper and lower wing as indicated by annotation B. The axial velocity increase is slightly higher for the PNWFR configuration because of the induced axial velocity by the propeller. Comparing the PNWFR and PN configuration, the axial velocity component just upstream of the propeller is lower on average for the installed case, likely due to the wake of the wings and change in flow direction to more tangential flow. The differences upstream of the propeller impact the slipstream of the propeller: The axial velocity component levels off to a slightly lower value.

Looking at the tangential velocity plot, a growth in negative tangential velocity component towards the propeller is present for the PNWFR and NWFR configuration, induced by the wing. Comparing the PNWFR and PN configuration results downstream of the propeller, the tangential velocity component is considerably lower for the installed case. Comparing the NWFR and PNWFR configuration results, the tangential velocity field around the wingtip has changed direction due to the propeller. As the tangential velocity magnitude is lower, the tangential kinetic energy in the slipstream has been reduced by the interaction.

From Figs. 7 through 10 it is clear that part of the wing experiences a different flowfield as a result of the propellers, in particular in axial velocity. Therefore, it can be expected that the wing loading may also change. As there is a finite number of propeller blades and the propellers rotate, they also introduce time-dependent variations in wing loading. To identify changes in wing lift and drag by the propellers, in Fig. 11 the time-averaged spanwise wing loading is plotted for the left wing half. Note that the right wing half experiences higher wing lift due to the reduced main rotor downwash on that side [8], but the interaction phenomena are similar. Results for the NWFR and PNWFR configurations are shown, including the

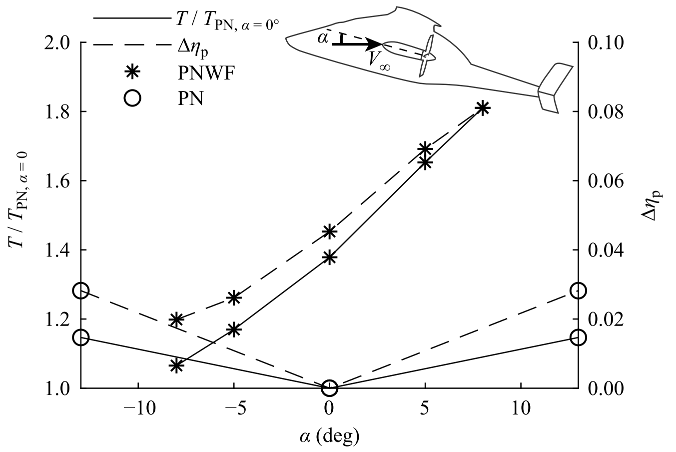

Fig. 12. Left propeller thrust T and propulsive efficiency $\eta_\mathrm{p} = (TV_\infty \cos\alpha)/P$ are plotted against angle of attack α at constant blade pitch angle for $V_\infty = 220$ kt (113.2 m/s). A comparison is shown between the PNWF and PN configuration and quantities are with respect to PN configuration quantities at zero angle of attack.

time-dependent variation indicated by the shaded areas. The propellers introduce locally a slight reduction in upper wing lift and larger increase in lower wing lift, as well as a time-dependent variation. Wing drag is increased locally for the upper and lower wing, resulting in a net reduction of lift-over-drag ratio. At spanwise locations away from the propeller, the effect of the propeller reduces.

Because of the strong aerodynamic interaction between the propellers and the box-wings, an investigation of the interaction for off-design conditions is essential to understand the flight performance and dynamics of this vehicle. The effects of angle of attack and sideslip were studied with the PNWF and PN configurations, leaving the main rotor effect out for this study. In Fig. 12 the left propeller performance is plotted as function of angle of attack. Results are made relative with the performance at zero angle of attack for the PN configuration. For the PN configuration, the thrust and propulsive efficiency increase with angle of attack, symmetrically around zero angle of attack. For the PNWF configuration, the wing introduces an increase in thrust and efficiency at zero angle of attack due to the tangential velocity field and wing wakes. Since the strength of the tangential velocity field is correlated to wing lift and wing lift increases with angle of attack, an increase in angle of attack increases thrust and efficiency more than for the isolated propeller. The symmetry around zero angle of attack is therefore also lost as a result of the aerodynamic interaction with the wing.

To show the effects of sideslip, the right propeller was studied with a positive sideslip angle to avoid significant fuselage interaction. In Fig. 13 the right propeller performance as function of sideslip is plotted for a reduced manoeuvring cruise speed. Again, at zero sideslip the thrust and efficiency are higher for the PNWF configuration compared to the PN configuration due to the effect of the wing. The difference in thrust and efficiency between the PNWF and PN configuration result gradually reduces with increasing sideslip as the wing lift reduces and thus the effect of the wing on the propeller reduces for the PNWF result. Note that the propeller is operating at a different advance ratio, such that with increasing angle of attack the efficiency for the PN configuration reduces already for small angles, opposite to the results of Fig. 12.

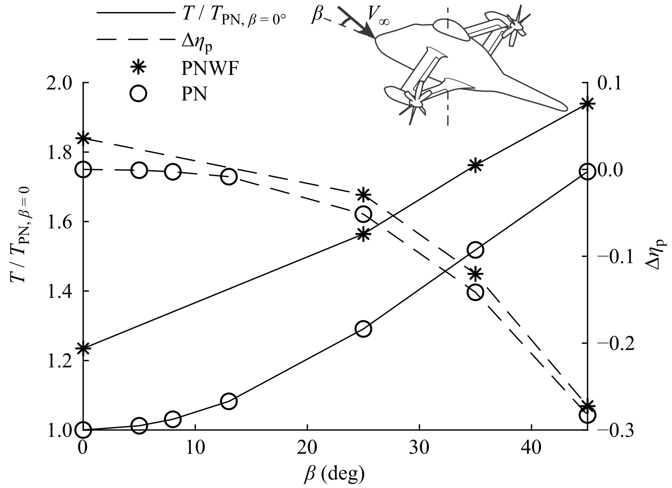

Fig. 13. Right propeller thrust T and propulsive efficiency $\eta_\mathrm{p} = (TV_\infty \cos\beta)/P$ are plotted against sideslip β at constant blade pitch angle for a reduced cruise speed for manoeuvring of $V_\infty = 140$ kt (72.0 m/s). A comparison is shown between the PNWF and PN configuration and quantities are with respect to PN configuration quantities at zero sideslip.

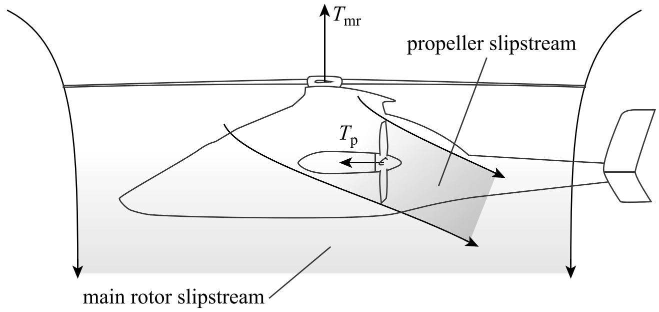

Fig. 14. Sketch of main rotor and propeller aerodynamic interaction in hover, indicating the direction of the main rotor thrust T_mr and propeller thrust T_p.

3.2. Hover condition

The main rotor plays only a minor role in the aerodynamic interactions experienced by the propellers in the cruise condition. However, the lack of shielding of the propellers allows for a significant main rotor interaction at low airspeed and particularly in the hover condition where the main rotor downwash impinges on the propellers, as sketched in Fig. 14. The flowfield through the left and right propeller is visualised in Fig. 15 for the PNWFR configuration by streamtraces with velocity contours and this figure indicates the large angle of attack experienced by the propellers. The velocity is made dimensionless with V_d, the theoretic farfield downwash velocity of the main rotor based on momentum theory $V_\mathrm{d} = \sqrt{\frac{2T_\mathrm{mr}}{\rho_\infty \pi R_\mathrm{mr}^2}}$ [29]. Note that, in order to counter the torque of the main rotor, the right propeller blade pitch angle is set to produce a reverse thrust in the hover condition. Not only the propellers but also the wings experience the very large negative angle of attack due to the main rotor downwash, resulting in a net download, as was also shown by Lynn [14]. This resulted in the choice of a box-wing design for the Airbus RACER, in order to reduce the overall surface affected by the downwash. It can be seen that the wings introduce additional disturbances to the inflow of especially the left propeller with unknown impact on the propeller loading. Since the right propeller is producing reverse thrust, the wings are in its slipstream, and the effect of the wings on this propeller are likely different. Because of these unknowns, the impact of this complex interactional flow on the propeller performance and unsteady aerodynamic loading was investigated.

To further illustrate the flowfield experienced by the left propeller, in Fig. 16 the velocity magnitude is plotted with streamlines on a plane through the propeller for the NWFR configuration, so

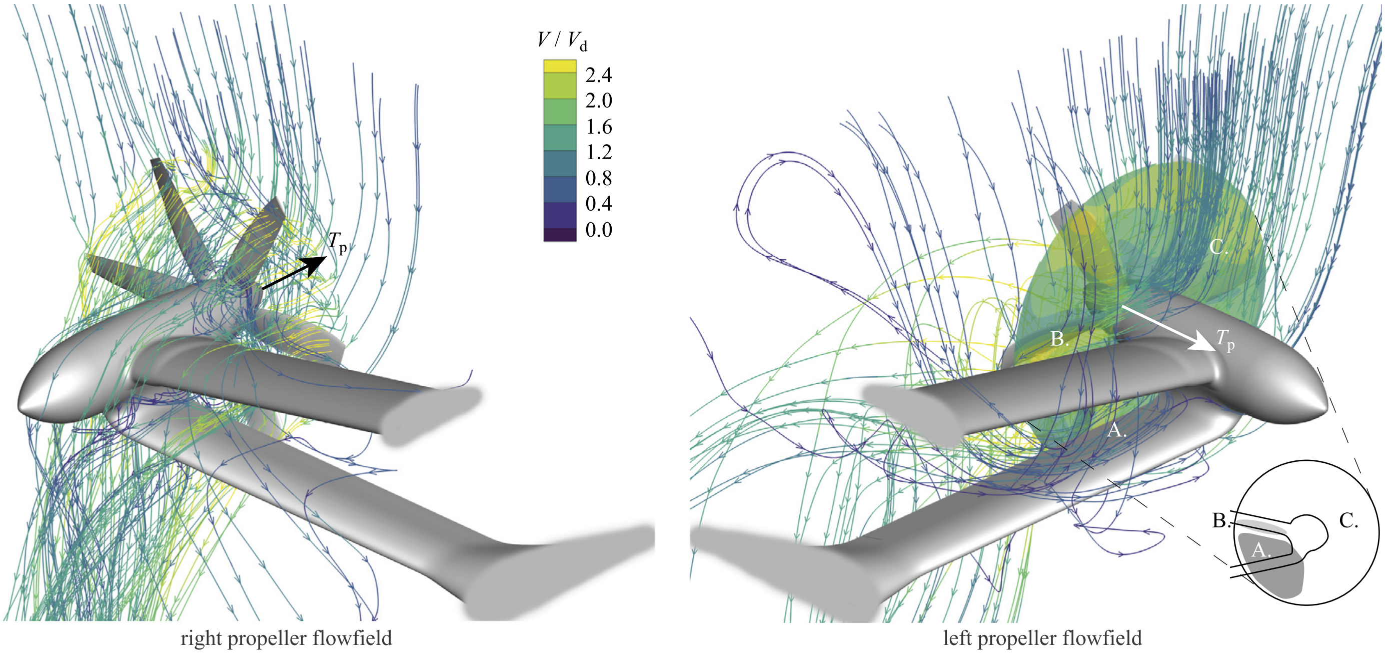

Fig. 15. For the PNWFR configuration in hover, the flow through the propellers is visualised, with velocity contours on streamtraces and on a plane $0.18R_p$ upstream of the left propeller. The fuselage is not shown. Annotation A. indicates the wake of the wings and nacelle, B. main rotor downwash deflected by upper wing and C. the area undisturbed by the wings.

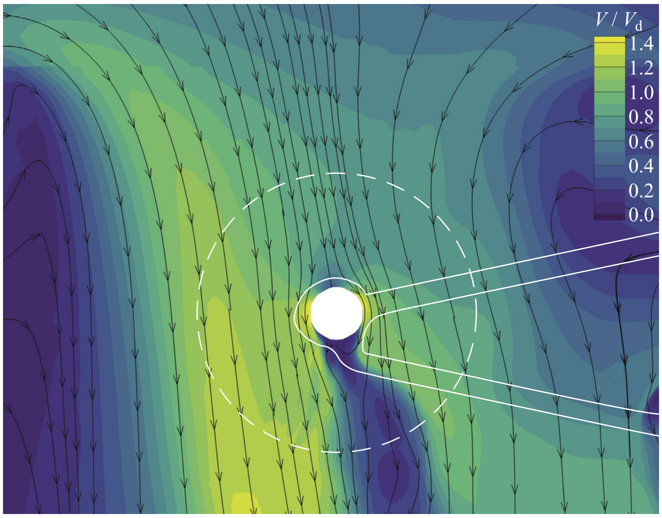

Fig. 16. The velocity field in a plane through the left propeller in hover is shown for the NWFR configuration, so without propeller present.

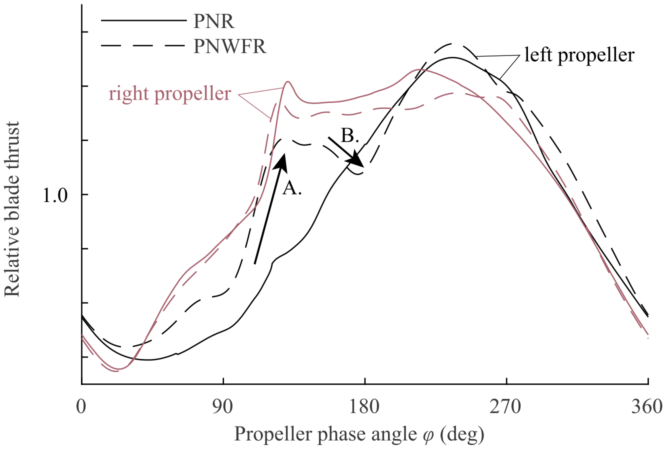

Fig. 17. Blade thrust is plotted relative to the time-averaged blade thrust during a full rotation in hover for the PNR and PNWFR configuration. Phase angle φ is defined in Fig. 1 and the quantities are plotted divided through the PNWFR time-averaged value. Annotation A. indicates the effect of the wake of the wings and nacelle and B. the effect of main rotor downwash deflected by the upper wing.

without propellers present. The propeller will experience a non-uniform distribution of downwash by the main rotor. Furthermore, an area of reduced velocity on the lower side of the nacelle can be distinguished. This wake is formed because the nacelle is shielding this area from the main rotor downwash. Considering that the wake is more pronounced on the inboard side of the nacelle, the shielding of the main rotor downwash by the wings likely also plays a role in the development of this wake. The flowfield in this plane at the location of the right propeller is very similar, since the main rotor loading is equal on both sides in the hover condition. The main difference is the out-of-plane swirl component introduced by the main rotor, which cannot be observed in this figure.

To establish a quantitative indication of the aerodynamic interaction effects, simulations were performed with the propeller-nacelle-main rotor configuration PNR and nacelle-wing-fuselage-main rotor configuration NWFR and were compared to results of the complete configuration PNWFR. Differences in integral propeller loading were found: Although the blade pitch angle and all other operating conditions were kept constant between the PNR and PNWFR configuration, for the left propeller the thrust in the PNWFR configuration was found to be 10.5% higher. This difference is therefore likely a result of the role the wings play in the interaction. The thrust-over-power ratio T/P for the left propeller in the PNWFR configuration was slightly reduced, although this could be directly a result of the increased thrust. Contrary, for the right propeller the thrust was 1.5% reduced in the PNWFR configuration and the thrust-over-power ratio did not significantly change between the two configurations.

In order to investigate the differences between the propeller blade loading for the PNR and PNWFR configuration, in Fig. 17 the blade thrust evolution over a complete rotation is plotted for the

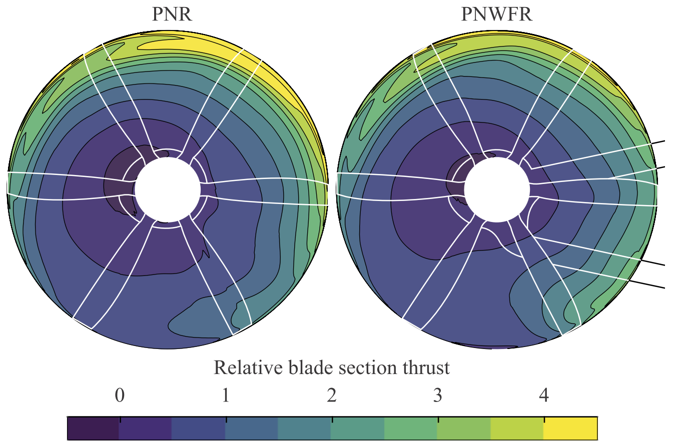

Fig. 18. The blade section thrust relative to the time-averaged blade thrust is plotted for each circumferential position of the left propeller in hover. The effect of the wings is shown by means of comparison of the PNR and PNWFR configuration at equal blade pitch angle.

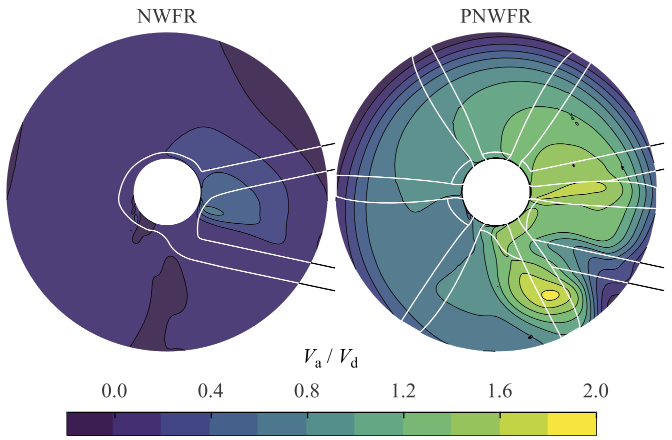

Fig. 19. Time-averaged axial velocity component is plotted on the plane visualised in Fig. 15, upstream of the left propeller in hover. The effect of the propeller is shown by means of comparison of the NWFR and PNWFR configuration.

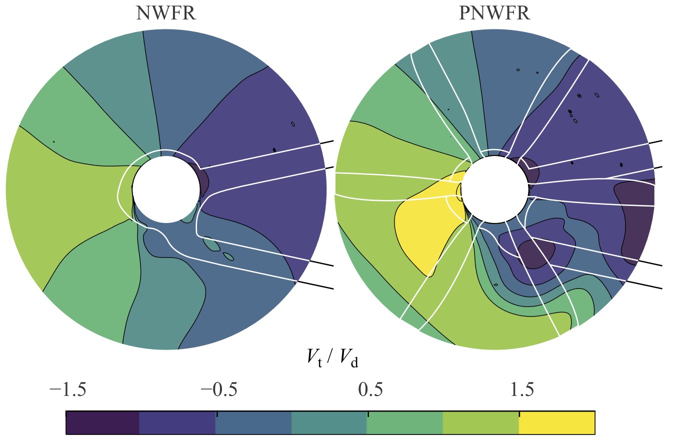

Fig. 20. Time-averaged tangential velocity component is plotted corresponding to Fig. 19.

left and right propeller, both relative to the time-averaged blade loading for the PNWFR configuration. Although not quantified in the figure, the peak-to-peak variation in blade thrust is very significant. For the left propeller the peak-to-peak variation is approximately equal to 60% of the maximum required thrust in hover for counter-torque (left propeller 100% thrust, right propeller 0% thrust), but note that this plotted case is not the maximum thrust requiring case. In general, the loading evolution is approximately sinusoidal for both propellers in both configurations. The phase and amplitudes of the PNR and PNWFR result are very similar for both propellers. Note that although for the PNR configuration no wings and fuselage are present, the blade loading evolution is not perfectly sinusoidal for either propeller, which is normally expected for a propeller at angle of attack. This is likely related to the non-uniformity in the main rotor downwash that was illustrated in Fig. 16. When the wings are present, for the left propeller a significantly increased thrust is noticeable in between $\varphi = 90$ deg and 160 deg, indicated by annotation A., after which a relative reduction of thrust occurs indicated by annotation B.

For the right propeller the differences between the PNR and PNWFR configuration results are very small. This is thought to be, because the wings are in the slipstream of the propeller and do not significantly disturb the inflow to the propeller. However, a small thrust decrease is noticeable between $\varphi = 130$ deg and 270 deg, when the blade moves behind and above the wings. A small local angle of attack reduction induced by the wings could have caused this thrust reduction.

For the left propeller the differences between the PNR and PNWFR configuration are larger than for the right propeller and therefore require further investigation. Fig. 18 allows correlation of the thrust variation with the wing location for the left propeller through contour plots of the blade section thrust for the PNR and PNWFR configuration. This figure should be viewed alongside Figs. 19 and 20, which show a comparison of the axial and tangential velocity distribution for the NWFR and PNWFR configuration, so without and with propeller respectively. These contours are plotted on the plane visualised in Fig. 15 (right) just upstream of the left propeller, when seen from behind. Note that in this figure also a front view sketch is made of the propeller disk and a division is made in three zones annotated A., B. and C. An explanation of the propeller loading for each zone is given in the following paragraphs.

In zone A. the propeller in the PNWFR configuration draws air from the wake of the nacelle and wings that was made visible in Fig. 16. In Fig. 19 indeed an almost zero axial velocity component can be observed in this area when the propeller is not present in the NWFR configuration. The almost static inflow condition results in a large angle of attack for the propeller blade sections and thus high thrust, explaining the sudden thrust increase from $\phi = 90$ deg to 160 deg compared to the PNR configuration. In Fig. 19 a peak in axial velocity for the PNWFR configuration is visible in this area, induced by the propeller as a result of the high thrust. Note that also a large negative tangential velocity component is induced by the propeller in this area, shown in Fig. 20. Typical of a propeller operating at static condition is that air is drawn to it from its wider surroundings and this is also clearly visible in Fig. 15, where a spanwise flow is visible in between the wings from inboard towards the propeller at its outboard location. The formation of the negative tangential velocity component upstream of the propeller may be a result of the lower wing guiding the propeller induced flow in that tangential direction.

In zone B. an area of positive axial velocity can be noticed in the NWFR result of Fig. 19, which is a result of the deflection of the main rotor downwash by the upper wing towards the propeller. This deflection can also be observed by the streamtraces in Fig. 15. This effect of the upper wing on the axial velocity is noticeable in the thrust distribution plot in Fig. 18 by a local reduction in thrust, as also previously identified in the blade loading evolution from $\phi = 160$ deg onwards. The axial velocity inflow reduces the angle of attack of the propeller blade sections and thus reduces thrust. Therefore, in the PNWFR result of Fig. 19, although an additional increase in axial velocity by the propeller is seen in this area, it is of lower magnitude than in zone A.

In zone C. no large differences between the PNWFR and PNR configuration in terms of propeller thrust are noticeable. The inflow to the propeller is free of objects for both configurations and operates in a way typical of a propeller at angle of attack. The increased integrated propeller thrust of 10.5% in the PNWFR configuration, which was mentioned earlier, should therefore be explained by the effects in zone A. and B. Apparently, the thrust increasing effect of the wake is stronger than the thrust decreasing effect by the deflection of the main rotor downwash by the upper wing, resulting in a net thrust increase due to the presence of the wings.

4. Conclusions

As part of the Clean Sky 2 (CS2) research programme, aerodynamic interactions occurring for the Airbus RACER (Rapid And Cost-Effective Rotorcraft) were investigated in a cruise and hover condition. A breakdown was presented of the aerodynamic interactions between the lateral rotors or propellers, the box-wings and the main rotor, focussing mainly at the effects on the propeller loading.

Since the propellers of this compound helicopter are situated below the main rotor and the main rotor slipstream passes over propellers in the cruise condition, the effect which the main rotor has on the propellers is limited to an angle of attack effect. A small negative angle of attack is induced to the inflow of the propellers, resulting in a sinusoidally varying propeller blade loading. Contrary, in the hover condition the direct impingement of the main rotor downwash on the propellers results in a very significant sinusoidally varying blade loading due to the inflow at almost perpendicular angle to the propeller axis. Any such compound helicopter layout where a propeller is situated below the main rotor would experience a similar interaction, if no other aerodynamic surfaces would be shielding it.

Since the propellers of this compound helicopter are located behind the wing at the wingtip, they ingest the rotational velocity field formed by the pressure difference between the upper and lower wing surfaces. Considering that the rotation direction of the propellers is against the rotation of the flow around the wingtip, an increase in thrust occurs. Furthermore, the low axial velocity of the wing wake is ingested, also resulting in a local propeller thrust increase. Comparison with the isolated propeller performance has led to the conclusion that installation increases propeller propulsive efficiency by 7% if the blade pitch is reduced to maintain equal thrust. The majority of this gain can likely be ascribed to the rotational flowfield. Due to the close proximity of the propeller to the wing, an upstream effect on the wing can however be expected. For this helicopter, the propellers increase wing lift, through a lift increase of the lower wing and a smaller lift decrease of the upper wing. The propellers increase drag of the upper and lower wings, thereby decreasing the wing lift-over-drag ratio.

This close coupling of propeller and wing loading has consequences for incidence angle effects, for instance during manoeuvres. For this helicopter, there is a strong positive correlation between wing lift and propeller thrust and efficiency in the cruise condition. This significantly changes angle of attack and sideslip angle effects compared to those of an isolated propeller.

Since in the hover condition the propellers on the Airbus RACER are used to counter the torque of the main rotor, an asymmetry arises between the left and right propeller. For the left propeller, the wing introduces disturbances to the inflow. This causes local changes in the sinusoidal propeller blade loading induced by the main rotor. The left upper wing deflects the main rotor downwash towards the left propeller, resulting in an axial velocity component which decreases locally the thrust. The wake formed by the nacelle and wings in the main rotor downwash causes the left propeller to locally operate similar to in static condition, drawing low momentum flow from the wake. This increases the thrust. Overall, the wings increase the left propeller thrust by 10.5% with slightly reduced thrust-over-power ratio for equal blade pitch. For the right propeller, the wings are in its slipstream. They lead to a decrease of right propeller reverse thrust by 1.5% with constant thrust-over-power ratio for equal blade pitch.

Although the presented results are very specific to the Airbus RACER geometry, in general very significant aerodynamic interaction effects can be expected when a main rotor, propellers and wing are in proximity to each other. A breakdown of aerodynamic interaction effects by leaving away parts of the geometry, as presented here, can provide the necessary insight into these effects.

Declaration of competing interest

The authors declare that they have no known competing financial interests or personal relationships that could have appeared to influence the work reported in this paper.

References

[1] H. Yeo, Design and aeromechanics investigation of compound helicopters, Aerospace Science and Technology 88 (2019) 158–173, https://doi.org/10.1016/j.ast.2019.03.010.

[2] H. Yeo, W. Johnson, Optimum design of a compound helicopter, Journal of Aircraft 46 (2009) 1210–1221, https://doi.org/10.2514/1.40101.

[3] J. Enconniere, J. Ortiz-Carretero, V. Pachidis, Mission performance analysis of a conceptual coaxial rotorcraft for air taxi applications, Aerospace Science and Technology 69 (2017) 1–14, https://doi.org/10.1016/j.ast.2017.06.015.

[4] Airbus, Airbus helicopters reveals racer high-speed demonstrator configuration, https://www.airbus.com/newsroom/press-releases/en/2017/06/Airbus-Helicopters-reveals-Racer-high-speed-demonstrator-configuration.html, 2017.

[5] C. Lienard, I. Salah el Din, T. Renaud, R. Fukari, RACER high-speed demonstrator: rotor and rotor-head wake interactions with tail unit, in: AHS International 74th Annual Forum & Technology Display, 2018.

[6] S.A. Andrews, R.E. Perez, Comparison of box-wing and conventional aircraft mission performance using multidisciplinary analysis and optimization, Aerospace Science and Technology 79 (2018) 336–351, https://doi.org/10.1016/j.ast.2018.05.060.

[7] T.C.A. Stokkermans, M. Voskuijl, L.L.M. Veldhuis, B. Soemarwoto, R. Fukari, P. Eglin, Aerodynamic installation effects of lateral rotors on a novel compound helicopter configuration, in: AHS International 74th Annual Forum & Technology Display, 2018.

[8] M. Wentrup, J. Yin, P. Kunze, T. Streit, J.-H. Wendisch, T. Schwarz, J.-P. Pinacho, K. Kicker, R. Fukari, An overview of DLR compound rotorcraft aerodynamics and aeroacoustics activities within the CleanSky2 NACOR project, in: AHS International 74th Annual Forum & Technology Display, 2018.

[9] J.C. Patterson Jr, G.R. Bartlett, Effect of a wing-tip mounted pusher turboprop on the aerodynamic characteristics of a semi-span wing, in: AIAA/SAE/ASME/ASEE 21st Joint Propulsion Conference, AIAA Paper 1985-1286, 1985, https://doi.org/10.2514/6.1985-1286.

[10] J.C. Patterson Jr, G.R. Bartlett, Evaluation of Installed Performance of a Wing-Tip-Mounted Pusher Turboprop on a Semispan Wing, Technical Paper 2739, NASA, Hampton, Virginia, 1987.

[11] J.M. Janus, A. Chatterjee, C. Cave, Computational analysis of a wingtip-mounted pusher turboprop, Journal of Aircraft 33 (1996) 441–444, https://doi.org/10.2514/3.46959.

[12] L.R. Miranda, J.E. Brennan, Aerodynamic effects of wingtip-mounted propellers and turbines, in: 4th Applied Aerodynamics Conference, AIAA Paper 1986-1802, 1986, https://doi.org/10.2514/6.1986-1802.

[13] L.J. Bain, A.J. Landgrebe, Investigation of Compound Helicopter Aerodynamic Interference Effects, Technical Report 67-44, USAAVLABS, 1967.

[14] R.R. Lynn, Wing-rotor interactions, Journal of Aircraft 3 (1966) 326–332, https://doi.org/10.2514/3.43742.

[15] A. Batrakov, A. Kusyumov, S. Mikhailov, G. Barakos, Aerodynamic optimization of helicopter rear fuselage, Aerospace Science and Technology 77 (2018) 704–712, https://doi.org/10.1016/j.ast.2018.03.046.

[16] I. Salah el Din, C. Lienard, R. Huot, R. Fukari, RACER high-speed demonstrator: tail unit vertical fin aerodynamic design, in: AHS International 74th Annual Forum & Technology Display, 2018.

[17] C. Öhrle, U. Schäferlein, M. Keßler, E. Krämer, Higher-order simulations of a compound helicopter using adaptive mesh refinement, in: AHS International 74th Annual Forum & Technology Display, 2018.

[18] J. Thiemeier, C. Öhrle, F. Frey, M. Keßler, E. Krämer, Aerodynamics and flight mechanics analysis of airbus helicopters' compound helicopter RACER in hover under crosswind conditions, CEAS Aeronautical Journal (2019), https://doi.org/10.1007/s13272-019-00392-3.

[19] J.W. Boerstoel, A. Kassies, J.C. Kok, S.P. Spekreijse, ENFLOW, a Full-Functionality System of CFD Codes for Industrial Euler/Navier-Stokes Flow Computations, Technical Publication TP 96286 U, NLR, 1996.

[20] O.J. Boelens, H. Ven, J.C. Kok, B.B. Prananta, Rotorcraft Simulations Using a Sliding-Grid Approach, Technical Publication NLR-TP-2008-779, NLR, 2008.

[21] M. Laban, J.C. Kok, B.B. Prananta, Numerical tools for contra-rotating open-rotor performance, noise and vibration assessment, in: 27th International Congress of the Aeronautical Sciences (ICAS 2010), Nice, France, September 2010, pp. 19–24.

[22] A.F. Antoniadis, D. Drikakis, B. Zhong, G. Barakos, R. Steijl, M. Biava, L. Vigevano, A. Brocklehurst, O. Boelens, M. Dietz, M. Embacher, W. Khier, Assessment of CFD methods against experimental flow measurements for helicopter flows, Aerospace Science and Technology 19 (2012) 86–100, https://doi.org/10.1016/j.ast.2011.09.003.

[23] E.W.M. Roosenboom, A. Stürmer, A. Schröder, Advanced experimental and numerical validation and analysis of propeller slipstream flows, Journal of Aircraft 47 (2010) 284–291, https://doi.org/10.2514/1.45961.

[24] B. Ortun, R. Boisard, I. Gonzalez-Martino, In-plane airloads of a propeller with inflow angle: prediction vs. experiment, in: 30th AIAA Applied Aerodynamics Conference, AIAA Paper 2012-2778, 2012, https://doi.org/10.2514/6.2012-2778.

[25] S. Wallin, A.V. Johansson, An explicit algebraic Reynolds stress model for incompressible and compressible turbulent flows, Journal of Fluid Mechanics 403 (2000) 89–132, https://doi.org/10.1017/S0022112099007004.

[26] F.R. Menter, Two-equation eddy-viscosity turbulence models for engineering applications, AIAA journal 32 (1994) 1598–1605, https://doi.org/10.2514/3.12149.

[27] I.B. Celik, U. Ghia, P.J. Roache, C.J. Freitas, H. Coleman, P.E. Raad, Procedure for estimation and reporting of uncertainty due to discretization in CFD applications, Journal of Fluids Engineering 130 (2008) 078001, https://doi.org/10.1115/1.2960953.

[28] P.J. Roache, Quantification of uncertainty in computational fluid dynamics, Annual Review of Fluid Mechanics 29 (1997) 123–160, https://doi.org/10.1146/annurev.fluid.29.1.123.

[29] W. Johnson, Helicopter Theory, Courier Corporation, 1994.